Radio-frequency pseudonull induced by light in an ion trap

Daun Chung,[1,2,3] Yonghwan Cha,[1,2,3] Hosung Shon,[1,2,3] Jeonghyun Park,[1,2,3] Woojun Lee,[1,2,4,*] Kyungmin Lee,[1,2,3] Beomgeun Cho,[1,2,3] Kwangyeul Choi,[1,2,3,5] Chiyoon Kim,[1,2,3,5] Seungwoo Yu,[1,2,3,5] Suhan Kim,[1,2,3,5] Uihwan Jeong,[1,2,3,5] Jiyong Kang,[1,2,3] Jaehun You,[1,2,3] and Taehyun Kim[1,2,3,4,5,6,†]

[1]*Department of Computer Science and Engineering, Seoul National University, Seoul 08826, South Korea*
[2]*Automation and Systems Research Institute, Seoul National University, Seoul 08826, South Korea*
[3]*NextQuantum, Seoul National University, Seoul 08826, South Korea*
[4]*Institute of Computer Technology, Seoul National University, Seoul 08826, South Korea*
[5]*Inter-University Semiconductor Research Center, Seoul National University, Seoul 08826, South Korea*
[6]*Institute of Applied Physics, Seoul National University, Seoul 08826, South Korea*

(Received 18 April 2025; accepted 20 June 2025; published 18 July 2025)

In a linear radio-frequency (rf) ion trap, the rf null is the point of zero electric field in the dynamic trapping potential where the ion motion is approximately harmonic. When displaced from the rf null, the ion is superimposed by fast oscillations known as micromotion, which can be probed through motion-sensitive light-atom interactions. In this work, we report on the emergence of the rf pseudonull, a locus of points where the ion responds to light as if it were at the true rf null, despite being displaced from it. The phenomenon is fully explained by accounting for the general two-dimensional structure of micromotion and is experimentally verified under various potential configurations, with observations in great agreement with numerical simulations. The rf pseudonull manifests as a line in a two-dimensional parameter space, determined by the geometry of the incident light and its overlap with the motional structure of the ion. The true rf null occurs uniquely at the concurrent point of the pseudonull lines induced by different light sources.

DOI: 10.1103/3dsq-47n7

I. INTRODUCTION

Ion trap systems are among the leading platforms for performing quantum computation [1–3] and simulations [4–6], owing to the stability of atomic internal states and the long coherence time of motional states within deep potentials [7,8]. In a linear radio-frequency (rf) ion trap, an oscillating quadrupole field provides confinement of motion within a two-dimensional plane through dynamic trapping [9]. Here the motion of an ion can effectively be separated into micromotion and secular motion [9,10]. Micromotion is the rapid motion oscillating at the frequency of the dynamic trapping field, which gives rise to a pseudopotential for secular motion at slower timescales. When the ion is at the rf null, the point of zero electric field, micromotion becomes negligible, and the secular motion can be approximated by harmonic motion. In multi-ion systems, these harmonic-oscillator states can mediate ion-ion interactions, serving as the basis for numerous quantum operations [11,12].

Numerous techniques for micromotion detection and compensation have been developed [10,13–21], primarily to minimize micromotion and position the ion at the rf null. Commonly, a simplified one-dimensional model of micromotion has been addressed [9,10,22], neglecting the combined structure of two-dimensional secular motion and micromotion in realistic potential configurations. A phenomenon that has remained largely unexplored due to this practice is the emergence of the rf pseudonull, a locus of points forming a line in space, where the ion interacts with light as if there were no micromotion, even when significantly displaced from the true rf null. Our work focuses on a comprehensive quantum-mechanical formulation of micromotion and its application to the experimental validation of the exact pattern of the rf pseudonull. The phenomenon can also be utilized as a practical method for the complete determination of the true rf null within the dynamic trapping plane when more than a single rf pseudonull line is observed simultaneously.

The paper is structured as follows. In Sec. II, a theory for the general two-dimensional structure of ion motion in a linear rf trap is developed. First, the classical approach is presented (Secs. II A and II B), followed by a quantum-mechanical treatment of the classical solution and its incorporation into the description of light-atom interactions (Sec. II C), where the rf pseudonull is shown to arise naturally from the spatial phase associated with the interaction (Sec. II D). In Sec. III, the experimental setup is introduced with emphasis on the configuration of electric fields and the geometry of laser beams. Section IV presents the experimental results alongside theoretical simulations, with a discussion of their implications. A summary is provided in Sec. V.

*Present address: Pasqal Korea, Seoul 06628, South Korea.
†Contact author: taehyun@snu.ac.kr

II. THEORY

In order to describe the general two-dimensional motion of a trapped ion, we apply the invariant method used for solving time-dependent oscillator systems [23–26]. Considering the case where there is an external force $\boldsymbol{F}(t)$ in addition to the trapping potential, the Hamiltonian of the radio-frequency trap is given as

$$H(t) = H_0(t) + V(t), \quad H_0(t) = \frac{\boldsymbol{p}^2}{2M} + \frac{1}{2}M\boldsymbol{x}^{\mathrm{T}}\boldsymbol{\Omega}^2(t)\boldsymbol{x},$$
$$V(t) = -\boldsymbol{F}(t)\cdot\boldsymbol{x}, \tag{1}$$

where $\boldsymbol{p}$ and $\boldsymbol{x}$ are the momentum and position operators, respectively, and the superscript T indicates the transpose of a vector. The curvature of the time-dependent potential is defined through the matrix $\boldsymbol{\Omega}^2(t) = (\omega_{\mathrm{rf}}^2/4)[\mathbf{A} + 2\mathbf{Q}\cos(\omega_{\mathrm{rf}}t)]$ [27], where $\mathbf{A}$ and $\mathbf{Q}$ are the curvature matrices generated by the static (dc) and rf potentials, respectively, whose components are given by

$$\mathbf{A}_{ij} = \frac{4Ze}{M\omega_{\mathrm{rf}}^2}\left(\frac{\partial^2\phi_{\mathrm{dc}}}{\partial x_i\partial x_j}\right), \quad \mathbf{Q}_{ij} = \frac{2Ze}{M\omega_{\mathrm{rf}}^2}\left(\frac{\partial^2\phi_{\mathrm{rf}}}{\partial x_i\partial x_j}\right). \tag{2}$$

The constant Z is the charge number ($Z = 1$ for most trapped ions), e is the elementary charge, M is the ion mass, and ω_{rf} is the rf angular frequency. We assume a conventional experimental configuration where the dc and rf potentials ϕ_{dc} and ϕ_{rf} are parametrized as

$$\phi_{\mathrm{dc}} = \frac{V_{\mathrm{dc}}}{2}[(\alpha-\beta)x'^2 - (\alpha+\beta)y'^2 + 2\beta z^2],$$
$$\phi_{\mathrm{rf}} = \frac{V_{\mathrm{rf}}}{2}\gamma(x^2 - y^2). \tag{3}$$

Here V_{dc} and V_{rf} are the dc and rf voltage amplitudes. The constraints imposed by the Laplace equation $\nabla^2\phi = 0$ are implicit in the curvatures α, β, and γ. In general, the dc field can be rotated within the radial plane via the transformation of the basis of $x' = \cos\theta x + \sin\theta y$ and $y' = -\sin\theta x + \cos\theta y$. We define the two motional modes within the xy plane as radial modes, and the mode confined by the static field in the z direction as the axial mode. Given Eq. (3), the axial mode can be neglected as it is decoupled from the dynamic field.

A. Secular-micromotion modes

Solving the classical equations of motion subject to the Hamiltonian $H_0(t)$ leads to a structure of secular-micromotion modes derived from the Mathieu equation [9]

$$\frac{d^2\boldsymbol{x}}{dt^2} + \boldsymbol{\Omega}^2(t)\boldsymbol{x} = \mathbf{0}. \tag{4}$$

Assuming an ansatz

$$\boldsymbol{f}(t) = e^{i(\lambda/2)\omega_{\mathrm{rf}}t}\sum_{n=-\infty}^{\infty} e^{in\omega_{\mathrm{rf}}t}\boldsymbol{b}_n, \tag{5}$$

we obtain the relation [27]

$$-\mathbf{D}_n\boldsymbol{b}_n + \boldsymbol{b}_{n-1} + \boldsymbol{b}_{n+1} = \mathbf{0}, \tag{6}$$

where $\mathbf{D}_n = \mathbf{Q}^{-1}[(2n+\lambda)^2\mathbf{I} - \mathbf{A}]$, with $\mathbf{I}$ the identity matrix. Stable solutions occur under the condition $|\boldsymbol{b}_0| \gg |\boldsymbol{b}_{\pm1}| \gg |\boldsymbol{b}_{\pm2}| \approx 0$. This results in the set of equations

$$-\mathbf{D}_0\boldsymbol{b}_0 + \boldsymbol{b}_{-1} + \boldsymbol{b}_{+1} = \mathbf{0}, \quad \boldsymbol{b}_{\pm1} = \mathbf{D}_{\pm1}^{-1}\boldsymbol{b}_0, \tag{7}$$

which can be expressed as a single equation as

$$\left(\mathbf{D}_0 - \mathbf{D}_{-1}^{-1} - \mathbf{D}_{+1}^{-1}\right)\boldsymbol{b}_0 = \mathbf{0}. \tag{8}$$

It can be seen that Eq. (8) not only determines the principal axes of the radial modes $\boldsymbol{b}_0$, but also $\boldsymbol{b}_{\pm1}$ through Eq. (7), which we define as micromotion modes. In the lowest-order approximation $\lambda \ll |2|$, we define $\mathbf{D}_1 \equiv \mathbf{D}_{\pm1} \approx \mathbf{Q}^{-1}(4\mathbf{I} - \mathbf{A})$, so Eq. (8) is reduced to an eigenvalue problem with respect to λ,

$$\left(\mathbf{D}_0 - 2\mathbf{D}_1^{-1}\right)\boldsymbol{b}_0 = \mathbf{0}, \tag{9}$$

which results in the diagonalization of the matrix $\mathbf{G} = \mathbf{A} + 2\mathbf{Q}\mathbf{D}_1^{-1}$. Then the solution can be obtained by taking the real part of

$$\boldsymbol{f}(t) = \sum_{m=1}^{2}\boldsymbol{b}^m(t)u_m e^{i\omega_m t},$$
$$\boldsymbol{b}^m(t) = \boldsymbol{b}_0^m + 2\cos(\omega_{\mathrm{rf}}t)\boldsymbol{b}_1^m$$
$$= \left(I + \frac{q}{2}\cos(\omega_{\mathrm{rf}}t)\mathbf{D}^{-1}\right)\boldsymbol{b}_0^m, \tag{10}$$

where u_m is the amplitude of mode m, $\omega_m = \lambda_m\omega_{\mathrm{rf}}/2$ and $\boldsymbol{b}_0^m$ are the secular frequencies and corresponding principal axes of mode m, respectively, and $\mathbf{D} \equiv (q/4)\mathbf{D}_1$, with $\boldsymbol{b}_1^m = \mathbf{D}_1^{-1}\boldsymbol{b}_0^m$ the corresponding vector of micromotion encoding both its direction and amplitude. Note that $q = 2eV_{\mathrm{rf}}\gamma/M\omega_{\mathrm{rf}}^2$ from Eqs. (2) and (3). We define the set of parameters $\{\omega_m, \boldsymbol{b}_0^m, \boldsymbol{b}_1^m\}$ as the secular-micromotion modes for mode m. In realistic experimental configurations where the dc potential is rotated, the off-diagonal terms of the matrix $\mathbf{D}_1$ are nonzero, so $\boldsymbol{b}_1^m$ is noncollinear to $\boldsymbol{b}_0^m$, which is a feature that is commonly overlooked in many studies on micromotion. Although it is straightforward to extend the formalism to include higher-order micromotion modes $\boldsymbol{b}_{\pm2}^m, \boldsymbol{b}_{\pm3}^m, \ldots$, their magnitude is computed to be negligible for typically occurring values of q within the range $0.1 < q < 0.3$.

B. Forced time-dependent oscillator

The particular solution to the classical equations of motion for mode m subject to the entire Hamiltonian $H(t) = H_0(t) + V(t)$ in Eq. (1),

$$\frac{d^2\boldsymbol{x}}{dt^2} + \boldsymbol{\Omega}^2(t)\boldsymbol{x} = \frac{\boldsymbol{F}(t)}{M}, \tag{11}$$

can be obtained by assuming an ansatz $\boldsymbol{x}_{\mathrm{p}}(t) = u_0^m(t)\boldsymbol{b}^m(t)$, which leads to the equation for $u_0^m(t)$,

$$\frac{d^2u_0^m}{dt^2} + \boldsymbol{\Omega}^2(t)u_0^m = \frac{\boldsymbol{F}(t)\cdot\boldsymbol{b}_0^m}{M}, \tag{12}$$

by taking the time average over one rf cycle, $\langle\cos(\omega_{\mathrm{rf}}\mathrm{t})\rangle = \langle\sin(\omega_{\mathrm{rf}}\mathrm{t})\rangle = 0$ and $\langle\cos^2(\omega_{\mathrm{rf}}\mathrm{t})\rangle = 1/2$. The solution to Eq. (12) can be expressed via the Green's-function method as

$$u_0^m(t) = u_0^m(0)\cos(\omega_m t) + \frac{1}{M\omega_m}\int_0^t dt' \sin[\omega_m(t-t')]\boldsymbol{F}(t')\cdot\boldsymbol{b}_0^m, \tag{13}$$

with the initial condition $u_0^m(0) = \boldsymbol{F}(0)\cdot\boldsymbol{b}_0^m/M\omega_m^2$. The initial condition is chosen so that for a constant force $\boldsymbol{F}(t) = \boldsymbol{F}_0$, we get $u_0^m(t) = u_0^m(0)$. Then, using Eqs. (10) and (13), the total classical solution can be expressed as [10]

$$\boldsymbol{x}_c(t) = \sum_{m=1}^{2}\boldsymbol{b}^m(t)\big[u_1^m\cos(\omega_m t) + u_0^m(t)\big]. \tag{14}$$

C. Quantum-mechanical description of micromotion

While quantization of the ion motion is not essential to elucidate the concept of the rf pseudonull, it establishes a complete theory, enabling exact numerical simulations in the presence of both thermal and coherent motion. The quantum-mechanical position operator of the radial modes corresponding to the classical solution in Eq. (14) is obtained as (see Appendixes A and B)

$$\boldsymbol{x}_q(t) = \sum_{m=1}^{2}\frac{\boldsymbol{b}^m(t)}{Z_m}x_0^m\{A_m^\dagger(t) + A_m(t) + 2\,\mathrm{Re}[\alpha_m(t)]\}, \tag{15}$$

where $\boldsymbol{b}^m(t)$ is the secular-micromotion mode vector from Eq. (10), $Z_m = |\boldsymbol{b}^m(0)|$ is a normalization constant, and $x_0^m = \sqrt{\hbar/2M\omega_m}$, with $\hbar$ the reduced Planck constant. The time-varying operators $A_m^\dagger(t)$ and $A_m(t)$ evolve as $A_m^\dagger(t) = e^{i\omega_m t}A_m^\dagger$ and $A_m(t) = e^{-i\omega_m t}A_m$, where $A_m^\dagger$ and A_m are the raising and lowering operators of a simple harmonic oscillator, respectively. The displacement caused by the force $\alpha_m(t)$, which is the coherent component of the motion, is obtained as

$$\alpha_m(t) = e^{-i\omega_m t}\alpha_m(0) + \frac{i}{\hbar}x_0^m\int_0^t dt' e^{-i\omega_m(t-t')}\boldsymbol{F}(t')\cdot\boldsymbol{b}_0^m, \tag{16}$$

subject to the initial condition $\alpha_m(0) = x_0^m\boldsymbol{F}(0)\cdot\boldsymbol{b}_0^m/\hbar\omega_m$ [26]. In our work, we limit our analysis to the case of static forces $\boldsymbol{F}(t) = \boldsymbol{F}(0)$; hence, $\alpha_m(t) = \alpha_m(0)$.

In order to rigorously incorporate the effects of micromotion into the light-atom interactions described by the Hamiltonian commonly used in ion trap systems [9],

$$H'_{\mathrm{LA}}(t) = \frac{\hbar\Omega}{2}(e^{i\boldsymbol{k}\cdot\boldsymbol{x}(t)}e^{-i\phi(t)}\sigma_+ + \mathrm{H.c.}), \tag{17}$$

we can simply replace $\boldsymbol{x}(t)$ in Eq. (17) with $\boldsymbol{x}_q(t)$ from Eq. (15) (see Appendix C). The parameters Ω, $\boldsymbol{k}$, and $\phi(t)$ are the Rabi frequency, wave vector, and phase associated with the external radiation field, respectively. The phase can be decomposed as $\phi(t) = \delta t + \phi_0$, where δ is the detuning and ϕ_0 is a phase offset. The operators σ_+ and its Hermitian conjugate (H.c.) σ_- are the raising and lowering operators of the internal two-level system. The Hamiltonian in Eq. (17) acts on a Hilbert space spanned by $\{|i\rangle\otimes|n_1\rangle_{A_1}\otimes|n_2\rangle_{A_2}\}$, where $i\in\{0,1\}$ is the index of the two-level system and $n_1, n_2 \in \{0,1,2,\ldots\}$ are the number-state bases of the harmonic oscillators, i.e., $A_m^\dagger|n_m\rangle_{A_m} = \sqrt{n_m+1}|n_m+1\rangle_{A_m}$.

D. Origin of the rf pseudonull induced by light

The rf pseudonull arises from the spatial phase term of the light-atom interaction described by Eq. (17), given as

$$\boldsymbol{k}\cdot\boldsymbol{x}_q(t) = \phi_{\mathrm{sm}}(t) + \phi_{\mathrm{mm}}(t), \tag{18}$$

where $\phi_{\mathrm{sm}}(t)$ is the harmonic-oscillator term that arises from secular motion,

$$\phi_{\mathrm{sm}}(t) = \sum_{m=1}^{2}\frac{\boldsymbol{k}\cdot\boldsymbol{b}_0^m}{Z_m}X_m(t),$$
$$X_m(t) = x_0^m\{A_m^\dagger e^{i\omega_m t} + A_m e^{-i\omega_m t} + 2\,\mathrm{Re}[\alpha_m(t)]\}, \tag{19}$$

and $\phi_{\mathrm{mm}}(t)$ is that which originates from micromotion, which can be further decomposed into the intrinsic and excess micromotion components,

$$\phi_{\mathrm{mm}}(t) = \phi_{\mathrm{in}}(t) + \phi_{\mathrm{ex}}(t),$$
$$\phi_{\mathrm{in}}(t) = 2\cos(\omega_{\mathrm{rf}}t)\sum_{m=1}^{2}\frac{\boldsymbol{k}\cdot\boldsymbol{b}_1^m}{Z_m}x_0^m(A_m^\dagger e^{i\omega_m t} + A_m e^{-i\omega_m t}),$$
$$\phi_{\mathrm{ex}}(t) = 2\cos(\omega_{\mathrm{rf}}t)\sum_{m=1}^{2}\frac{\boldsymbol{k}\cdot\boldsymbol{b}_1^m}{Z_m}x_0^m\mathrm{Re}[\alpha_m(t)]. \tag{20}$$

Since we only consider static displacements $\alpha_m(t) = \alpha_m(0)$, the stationary phase shift in $\phi_{\mathrm{sm}}(t)$ has no visible effect on the evolution of the system. In numerical simulations, the intrinsic part $\phi_{\mathrm{in}}(t)$ is neglected, $\phi_{\mathrm{in}}(t)\approx 0$, because it unnecessarily complicates the computation despite its small significance. Therefore, the primary time-dependent variation in the transition amplitude between the internal states of the two-level system is induced by the excess component $\phi_{\mathrm{ex}}(t)$. When the ion is in a highly thermal state, further variations result from thermal decoherence associated with the operators $A_m^\dagger$ and A_m in $\phi_{\mathrm{sm}}(t)$ [9]. In contrast, since $\phi_{\mathrm{ex}}(t)$ is a constant, the effect of micromotion is to induce a coherent phase modulation to the light-atom interaction through the factor $\exp[i\phi_{\mathrm{mm}}(t)] \approx \exp[i\phi_{\mathrm{ex}}(t)]$, which leads to displacement-dependent Rabi frequency variations.

Attributed to the contribution from the two modes, the net phase of $\phi_{\mathrm{ex}}(t)$ can cancel out, $\phi_{\mathrm{ex}}(t) = 0$, with the condition determined by the orientation of the wave vector $\boldsymbol{k}$ and its overlap with the ion's motional structure. From Eq. (20) it is algebraically clear that the locus satisfying this condition is not unique but forms a line in the two-dimensional displacement space. Along this line, micromotion is effectively hidden from the incident light, and the ion behaves as if it were a simple harmonic oscillator, even when superimposed with large micromotion. In Sec. IV, the cancellation of the spatial phase components is demonstrated to be coherent, leading to distinct signatures even when the ion is highly thermal. While it is geometrically intuitive that the rf pseudonull emerges as a line within the dynamic trapping plane, the description of the exact light-induced response of an ion undergoing two-dimensional micromotion is nontrivial without such theoretical understanding. The presented theory accurately predicts experimental rf pseudonull patterns for arbitrary potential configurations without relying on any free parameters. This becomes particularly important when the curvature matrices **A** and **Q** in Eq. (2) do not commute,

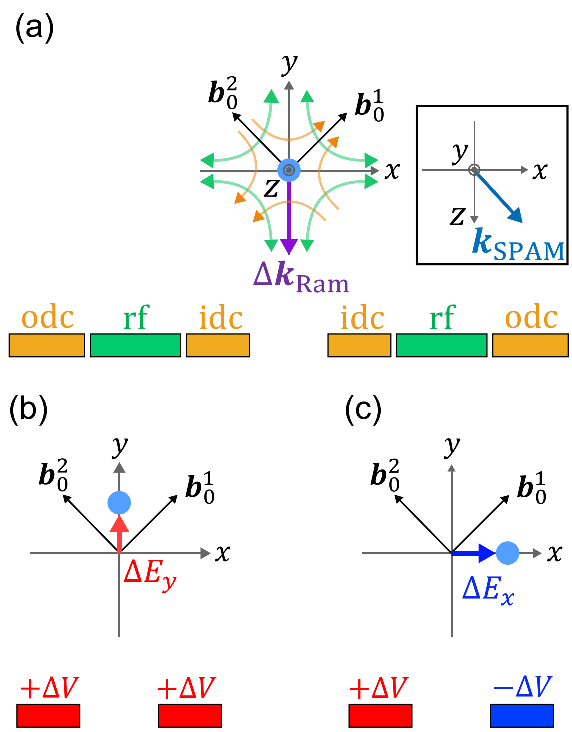

FIG. 1. Experimental configuration. (a) Cross section of the surface trap. The ion, represented by a blue circle at the origin of the coordinate system, is confined by the rf (green) and dc (orange) fields generated by the electrodes of the same color. The electrode labels idc and odc stand for inner and outer dc electrodes, respectively [30]. The principal axes of the radial modes $\boldsymbol{b}_0^m$ are rotated in the xy plane. In the inset $\Delta\boldsymbol{k}_{\rm Ram}$ and $\boldsymbol{k}_{\rm SPAM}$ are the wave vectors of the Raman beams and the Doppler/SPAM beam. Electric fields (b) ΔE_y and (c) ΔE_x are generated by applying symmetric ($+\Delta V$ and $+\Delta V$) and asymmetric ($+\Delta V$ and $-\Delta V$) voltages to the idc electrodes in order to shift the ion in the y and x directions, respectively.

which is an essential condition for operations with surface traps [28,29].

III. EXPERIMENTAL SETUP

The rf pseudonull is visualized through a series of experiments extended from the dc scanning method originally developed for the compensation of micromotion along the direction normal to the chip surface [19]. Dubbed the two-dimensional displacement scan, a single experimental sequence is executed in the following order. First, dc voltages are set to position the ion at the true rf null. Then the ion is displaced from the rf null within the xy plane by applying incremental voltages to the inner dc electrodes, as shown in Fig. 1. This amounts to applying a constant force to the ion through an external electric field, $\boldsymbol{F}(t) = e\Delta\boldsymbol{E}_0 = e(\Delta E_x\bar{\boldsymbol{x}} + \Delta E_y\bar{\boldsymbol{y}})$. At the new equilibrium position, the ion is Doppler cooled and the internal state is initialized to the state $|0\rangle = |\uparrow\rangle$. At each displacement, a motion-sensitive Rabi flopping is driven for a duration of $T = \pi/\Omega$ and tuned at the carrier frequency $\delta = 0$, after which the probability of the state $|1\rangle = |\downarrow\rangle$, $P_\downarrow$, is measured [19]. Away from the true rf null, micromotion increases and modulates the phase of light seen by the ion, given by $\phi_{\rm ex}(t)$ in Eq. (20), effectively modifying the Rabi frequency. The pattern of $P_\downarrow$ extracted when the displacement of the ion is scanned over a two-dimensional region is directly dependent on $\phi_{\rm ex}(t)$, with the orientation of light $\boldsymbol{k}$ most significantly altering the pattern. The result is independent of the Rabi frequency as long as it is much smaller than the secular frequencies $\Omega \ll \omega_1, \omega_2$.

The experiments are performed with a silicon-based microfabricated surface trap [30]. Hyperfine levels in the S orbital of the $^{171}\mathrm{Yb}^+$ ion, $|\uparrow\rangle = |^2S_{1/2}, F = 0, m_F = 0\rangle$ and $|\downarrow\rangle = |^2S_{1/2}, F = 1, m_F = 0\rangle$, are used as the internal states that undergo Raman transitions via two counterpropagating 355-nm beams derived from a mode-locked laser [31,32]. In this case, the wave vector $\boldsymbol{k}$ in Eq. (17) is replaced with $\Delta\boldsymbol{k}_{\rm Ram}$, the difference of the wave vectors from the two Raman beams, as shown in Fig. 1(a). The effective wave vector $\Delta\boldsymbol{k}_{\rm Ram} = -2\times(2\pi/\lambda_{355})\bar{\boldsymbol{y}}$ does not overlap with the z axis, making the Raman transition sensitive only to the radial motion of the ion. A 370-nm laser, referred to as the Doppler/SPAM beam, is used for Doppler cooling as well as state preparation and measurement (SPAM) [31]. Its orientation is given by the wave vector $\boldsymbol{k}_{\rm SPAM} = (2\pi/\lambda_{370})(\bar{\boldsymbol{x}} + \bar{\boldsymbol{z}})/\sqrt{2}$, as shown in the inset of Fig. 1(a). The main cooling transition occurs between the state $|\downarrow\rangle$ and a state $|e\rangle = |^2P_{1/2}, F = 0, m_F = 0\rangle$ in the P orbital [31].

IV. RESULTS

The results of the two-dimensional displacement scan are plotted in Fig. 2. Columns (a)–(e) display data obtained from different potential configurations, which are represented by the diagrams in row (0). The parameter values of α, β, and γ in Eq. (3) for each condition are provided in Appendix E. In the caption of Fig. 2, we specify the secular frequency of each mode, and the potential rotation angle θ, defined as the angle between the x axis and the principal axis $\boldsymbol{b}_0^1$. The mode $m = 1$ is designated as the mode with the smaller secular frequency, with its axis $\boldsymbol{b}_0^1$ emphasized by thicker lines in the diagrams. The numerical values of the secular-micromotion modes are also provided in Appendix E. Throughout Figs. 2(a)–2(d), the dc potential parameters are varied while the rf potential parameters are kept constant. In Fig. 2(e), on the other hand, the dc potential parameters are identical to those in Fig. 2(d), while the rf voltage amplitude is reduced. In all cases, $\omega_{\rm rf} = 2\pi \times 22.14$ MHz.

Row (1) of Fig. 2 exhibits simulation data of the two-dimensional scan. At each displacement set by the electric field $\boldsymbol{E}_0 = \Delta E_x\bar{\boldsymbol{x}} + \Delta E_y\bar{\boldsymbol{y}}$, the ion evolves from an initial state $|\psi(t=0)\rangle = |\uparrow\rangle \otimes |0\rangle_{A_1} \otimes |0\rangle_{A_2}$. Distinct global patterns, dependent on the experimental geometry, are predicted to occur and are clearly observed experimentally, as displayed in row (2) of Fig. 2. A key feature is the emergence of the rf pseudonull line, a continuous set of points where $\phi_{\rm ex}(t) = 0$, indicated by purple dashed lines. The maximal values of the excitation probability $P_{\downarrow,\rm Ram}$ are distributed along this line. Note that we indicate $P_\downarrow$ occurring from the Raman transition as $P_{\downarrow,\rm Ram}$ in order to distinguish it from the excitation probability associated with the Doppler/SPAM beam, $P_{\downarrow,\rm SPAM}$, introduced later. A Bessel-type pattern occurs in $P_{\downarrow,\rm Ram}$ with respect to this pseudonull line, even when the

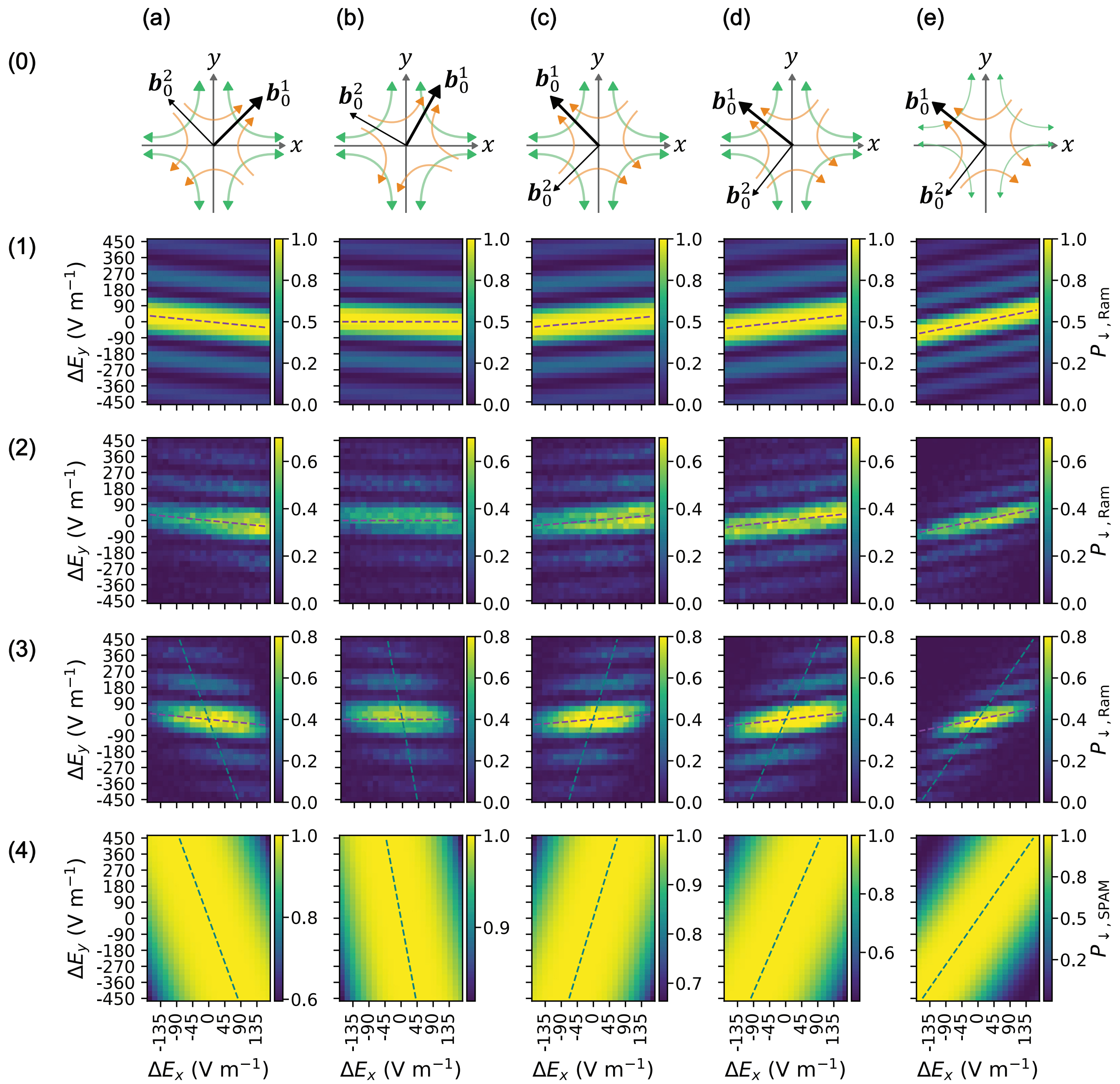

FIG. 2. Results of the two-dimensional displacement scan. Columns (a)–(e) group results based on different potential configurations, while rows (0)–(4) categorize data obtained under identical conditions. For each column, the secular frequencies and potential rotation angles are (a) $\{\omega_1, \omega_2\}/2\pi = \{1.79(0), 2.14(6)\}$ MHz and $\theta \approx \pi/4$, (b) $\{\omega_1, \omega_2\}/2\pi = \{1.87(4), 2.07(3)\}$ MHz and $\theta \approx \pi/3$, (c) $\{\omega_1, \omega_2\}/2\pi = \{1.82(0), 2.12(1)\}$ MHz and $\theta \approx 3\pi/4$, (d) $\{\omega_1, \omega_2\}/2\pi = \{1.75(6), 2.22(6)\}$ MHz and $\theta \approx 7\pi/9$, and (e) $\{\omega_1, \omega_2\}/2\pi = \{1.26(8), 1.88(2)\}$ MHz and $\theta \approx 7\pi/9$. Only the dc voltages have been varied in (a)–(d), while in (e), the rf voltage amplitude has been reduced by a factor of 0.8, keeping the dc voltages identical to those in (d). Row (0) shows the schematic depiction of potential configurations. The data in the subsequent rows are given as follows: (1) simulations of the scan under constant Rabi drives via Raman transitions, plotting $P_{\downarrow,\mathrm{Ram}}$; experimental data of the scan with the Doppler/SPAM beam detuned by (2) -22 MHz and (3) -10 MHz from the cooling transition during Doppler cooling [note that the color bar maxima in rows (2) and (3) are set to 0.7 and 0.8, respectively, to enable a comparison of the relative Raman transition strengths for each case]; and (4) simulation of the scan conducted with the Doppler/SPAM beam, plotting $P_{\downarrow,\mathrm{SPAM}}$. The theoretical rf pseudonull lines induced by the Raman beams and Doppler/SPAM beam are represented by purple and teal dashed lines, respectively.

ion motion is highly thermal, due to the nature of coherent sinusoidal phase modulation [19,33,34].

The experimental data in rows (2) and (3) of Fig. 2 are acquired under identical conditions, but with the Doppler/SPAM beam detuned by −22 and −10 MHz from the cooling transition during Doppler cooling, respectively. The former enables a relatively uniform cooling condition throughout the region since the detuning is set to the rf frequency, efficiently cooling the ion via micromotion sidebands [10,35]. The latter, on the other hand, corresponds to the optimal Doppler cooling condition [10,35,36], given the linewidth of the cooling transition of approximately 20 MHz. Here the ion is cooled down to states with smaller mean phonon numbers, leading to higher values of $P_{\downarrow,\mathrm{Ram}}$ around the true rf null compared to the former, due to less thermal motional decoherence [37]. However, we observe that the signals become localized in a manner that is not fully accounted for by the simulation results in row (1) of Fig. 2.

This secondary feature actually originates from a different rf pseudonull line induced by the Doppler/SPAM beam, given by the geometry in Fig. 1(a). With the two-level states defined as $|0\rangle = |\downarrow\rangle$ and $|1\rangle = |e\rangle$ and the wave vector replaced with that of the 370-nm laser, $\boldsymbol{k}_{\mathrm{SPAM}}$, Eq. (17) describes the system Hamiltonian involved in a dissipative scattering process [38–40]. Neglecting scattering, we simulate the two-dimensional displacement scan with respect to the Doppler/SPAM beam, whose results are shown in row (4) of Fig. 2. Here $P_{\downarrow,\mathrm{SPAM}}$ is equivalent to the excitation probability of the state $|e\rangle$, P_e, which is a measure of fluorescence intensity. The subscript $\downarrow$ is used to reflect the experimental aspect that the standard state detection scheme distinguishes the state $|\downarrow\rangle$ from $|\uparrow\rangle$ by collecting fluorescence emitted during near-resonant driving of the cooling transition [31]. Note that the quantity $\epsilon = 1 - P_{\downarrow,\mathrm{SPAM}}$ does not correspond to the detection probability of the state $|\uparrow\rangle$ but rather the detection error associated with the loss of fluorescence due to altered transition strengths between the states $|\downarrow\rangle$ and $|e\rangle$ by micromotion. In Appendix D we discuss the general situation where scattering is present, in contrast to simulations involving only the system Hamiltonian, and present experimental results of the two-dimensional displacement scans of $P_{\downarrow,\mathrm{SPAM}}$ conducted identically to that of $P_{\downarrow,\mathrm{Ram}}$. In Fig. 2 row (4), the rf pseudonull induced by the Doppler/SPAM beam is indicated by teal dashed lines. In the region with high-$P_{\downarrow,\mathrm{SPAM}}$ values, the ion scatters more photons, resulting in more effective Doppler cooling to lower temperatures [41] and higher detection fidelity [31].

There is a more direct way to observe the pseudonull line induced by the Doppler/SPAM beam through a commonly used micromotion compensation technique, typically termed photon correlation [13,16]. We conduct a two-dimensional displacement scan, where the visibility from a photon correlation experiment is extracted and plotted at each point. The visibility, defined as $(I_{\max} - I_{\min})/(I_{\max} + I_{\min})$, with $I_{\max}$ and $I_{\min}$ denoting the maximum and minimum photon counts recorded over one rf oscillation period, serves as an indicator of micromotion seen by the laser. The experimental result, obtained under the potential configuration in Fig. 2(c), is presented in Fig. 3(a). Here we clearly see the rf pseudonull line as the locus of data points where the visibility reaches zero.

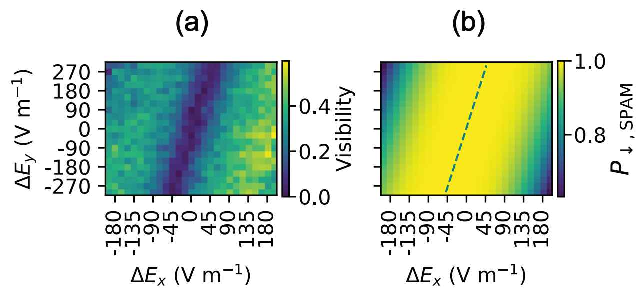

FIG. 3. Two-dimensional displacement scan conducted with the Doppler/SPAM beam. (a) Visibility extracted from photon correlation experiments. (b) Simulation results of the Hamiltonian in Eq. (17) acting on the two-level system with $|0\rangle = |\downarrow\rangle$, $|1\rangle = |e\rangle$, and $\boldsymbol{k}$ replaced by $\boldsymbol{k}_{\mathrm{SPAM}}$.

This is in agreement with simulation data, shown in Fig. 3(b), where the rf pseudonull line induced by the Doppler/SPAM beam is indicated by a dashed line. The pseudonull line appears sharper in Fig. 3(a) because, while the photon correlation method directly probes the strength of micromotion, the Hamiltonian simulation results in Fig. 3(b) show how the excitation probability is modified in the presence of micromotion.

It follows that the data in row (3) of Fig. 2 visualizes the combined pattern of the two rf pseudonull lines induced by both the Raman and Doppler/SPAM beams, with the influence of $P_{\downarrow,\mathrm{SPAM}}$ implicitly reflected in $P_{\downarrow,\mathrm{Ram}}$ through the SPAM fidelity, which manifests as a gradual fading of signals at the edges of the high-$P_{\downarrow,\mathrm{SPAM}}$ region. The true rf null lies at the common intersection of the pseudonull lines induced by the different beams. This concurrent point, tuned to $\Delta E_x = \Delta E_y = 0$, is indeed where the highest excitation probability $P_{\downarrow,\mathrm{Ram}}$ occurs empirically, under the optimal Doppler cooling condition. Our results imply that performing the two-dimensional displacement scan can uniquely identify the true rf null, provided that at least two pseudonull lines are observed. These pseudonull lines do not necessarily have to be induced by mutually orthogonal beams, as the localization of signals occurs at the concurrent point as long as they are noncollinear. This serves as a fully self-contained method that achieves complete determination of the true rf null in the radial plane using optical excitations of a single ion, requiring no supplementary techniques.

In addition, the two-dimensional displacement scan can be utilized for the calibration and characterization of potential configurations *in situ*, employing lasers used for routine operations. [19]. The experimental data visualize the dc potential rotation and the rf field strength through the landscape of $P_{\downarrow,\mathrm{Ram}}$ and also allow assessment of the robustness of the configuration against thermal motion and micromotion, with potential applications for various quantum operations [42,43] and precision metrology [44,45]. For instance, the Doppler cooling efficiency can be inferred from the excitation probability as a function of the dc potential rotation angle, as shown in Figs. 2(b)–2(d), where greater rotation leads to higher values of $P_{\downarrow,\mathrm{Ram}}$, implying lower Doppler limit temperatures. Also, the variation in the area of the rf pseudonull with rf field strength, as shown in Figs. 2(d) and 2(e), enables estimation of the system's susceptibility to excess micromotion induced by stray electric fields in arbitrary directions.

V. CONCLUSION

To summarize, we introduced the notion of the rf pseudonull, a phenomenon overlooked in ion trap systems due to an insufficient understanding of the general two-dimensional ion motion beyond the pseudopotential regime. A quantum-mechanical theory was developed from classical solutions, capable of describing both micromotion and thermal motion within a unified framework. Our theory accurately predicted the emergence of the rf pseudonull as a consequence of coherent light-atom interactions, consistent with observations from the two-dimensional displacement scan experiments. The extraction of global patterns serves as an experimentally feasible method for locating the true rf null at the common intersection of multiple pseudonull lines, requiring at minimum a single motion-sensitive beam in addition to the primary beam used for mandatory SPAM operations.

ACKNOWLEDGMENTS

This work was supported by the Institute for Information & Communications Technology Planning & Evaluation (IITP) Grant No. RS-2022-II221040 and the National Research Foundation (NRF) of Korea Grants No. RS-2020-NR049232, No. RS-2024-00442855, and No. RS-2024-00413957, all of which are funded by the Korean government (MSIT).

DATA AVAILABILITY

The data that support the findings of this article are not publicly available. The data are available from the authors upon reasonable request.

APPENDIX A: QUANTIZATION OF SECULAR-MICROMOTION MODES

We review the invariant method applied to the quantum-mechanical description of an undriven one-dimensional trapped ion [25], in which case the Hamiltonian is reduced to

$$H_0(t) = \frac{p_x^2}{2M} + \frac{1}{2}M\Omega_x^2(t)x^2,$$
$$\Omega_x^2(t) = \frac{\omega_{\rm rf}^2}{4}[a_x + 2q_x\cos(\omega_{\rm rf}t)]. \quad \text{(A1)}$$

The position operator in the Heisenberg picture is obtained as [46]

$$x(t) = \sqrt{\frac{\hbar g_-(t)}{2\omega_x}}(e^{i\omega(t)}a_x^\dagger + e^{-i\omega(t)}a_x), \quad \text{(A2)}$$

where ω_x is the invariant of the system and $g_-(t) = |f(t)|^2/M$ is obtained from the classical solution of the one-dimensional system $f(t)$ in Eq. (10), subject to the initial condition $f(0) = 1$ and $\dot{f}(0) = i\omega_x$ [24]:

$$f(t) = e^{i\omega_x t}\frac{1 + \frac{q_x}{2}\cos(\omega_{\rm rf}t)}{1 + \frac{q_x}{2}}. \quad \text{(A3)}$$

The term $\omega(t)$, obtained as

$$\omega(t) = \omega_x\int_0^t dt'\frac{1}{Mg_-(t')}, \quad \text{(A4)}$$

is reduced to $\omega(t) = \omega_x t$ when the terms resulting in factors of q_x^2 are approximated to 1, i.e., $|f(t)|^2 \approx 1$. In this limit, the expression in Eq. (A2) becomes

$$x(t) = \left(\frac{1 + \frac{q_x}{2}\cos(\omega_{\rm rf}t)}{1 + \frac{q_x}{2}}\right)x_0(e^{i\omega_x t}a_x^\dagger + e^{-i\omega_x t}a_x), \quad \text{(A5)}$$

where $x_0 = \sqrt{\hbar/2M\omega_x}$. This corresponds to the classical solution upon taking the expectation value

$$\langle u_x|x(t)|u_x\rangle \propto \left(1 + \frac{q_x}{2}\cos(\omega_{\rm rf}t)\right)\cos(\omega_x t) \quad \text{(A6)}$$

up to an amplitude where $|u_x\rangle$ is a coherent state defined through $a_x|u_x\rangle = u_x|u_x\rangle$. We can use this classical-quantum correspondence to naturally extend the solution in Eq. (A5) to two- and three-dimensional systems, by constructing a position operator whose expectation value with respect to a multimode coherent state is reduced to the classical solution. Without loss of generality, the position operator of the radial modes of the Hamiltonian $H_0(t)$ in Eq. (1) can be defined as

$$\boldsymbol{x}(t) = \sum_{m=1}^{2}\frac{\boldsymbol{b}^m(t)}{Z_m}x_0^m(e^{i\omega_m t}a_m^\dagger + e^{-i\omega_m t}a_m), \quad \text{(A7)}$$

where $x_0^m = \sqrt{\hbar/2M\omega_m}$, with $\hbar$ the reduced Planck constant, and $Z_m = |\boldsymbol{b}^m(0)| = |\boldsymbol{b}_0^m + 2\boldsymbol{b}_1^m|$ is a normalization constant that normalizes the solution such that $|\boldsymbol{f}(0)| = 1$. Note that $a_m^\dagger$ and a_m are the raising and lowering operators of an undriven time-dependent oscillator and should be distinguished from the corresponding operators $A_m^\dagger$ and A_m, introduced in Appendix B for the driven case.

APPENDIX B: FORCED TIME-DEPENDENT OSCILLATOR IN THE HEISENBERG PICTURE

The quantum-mechanical position operator in the presence of an external force, subject to the total Hamiltonian $H(t)$ in Eq. (1), can be derived in two different ways. The first is based on the invariant approach [26], where we introduce displaced raising and lowering operators $A_m^\dagger(t) = a_m^\dagger(t) - \alpha_m^*(t)$ and $A_m(t) = a_m(t) - \alpha_m(t)$, in terms of which Eq. (A7) can be extended as

$$\boldsymbol{x}_{\rm q}(t) = \sum_{m=1}^{2}\frac{\boldsymbol{b}^m(t)}{Z_m}x_0^m\{A_m^\dagger(t) + A_m(t) + 2\,{\rm Re}[\alpha_m(t)]\}. \quad \text{(B1)}$$

Under the approximation $|\boldsymbol{f}(t)|^2 \approx 1$, the raising and lowering operators are obtained as $A_m^\dagger(t) = e^{i\omega_m t}A_m^\dagger$ and $A_m(t) = e^{-i\omega_m t}A_m$, while the displacement caused by the force, $\alpha_m(t)$, which is the coherent component of the motion, obeys the equation

$$\frac{d\alpha_m}{dt} + i\omega_m\alpha_m = \frac{i}{\hbar}x_0^m\boldsymbol{F}(t')\cdot\boldsymbol{b}_0^m, \quad \text{(B2)}$$

resulting in the solution

$$\alpha_m(t) = e^{-i\omega_m t}\alpha_m(0) + \frac{i}{\hbar}x_0^m\int_0^t dt' e^{-i\omega_m(t-t')}\boldsymbol{F}(t')\cdot\boldsymbol{b}_0^m, \quad \text{(B3)}$$

with the initial condition $\alpha_m(0) = x_0^m\boldsymbol{F}(0)\cdot\boldsymbol{b}_0^m/\hbar\omega_m$ [26]. It can be seen that the expectation value of $\boldsymbol{x}_\mathrm{q}(t)$ with respect to the two-mode coherent state $|u_1u_2\rangle_A = |u_1\rangle_{A_1}\otimes|u_2\rangle_{A_2}$ results in the classical solution $\boldsymbol{x}_\mathrm{c}(t)$ in Eq. (14) up to an amplitude $\langle u_1u_2|_A\boldsymbol{x}_\mathrm{q}(t)|u_1u_2\rangle_A \propto \boldsymbol{x}_\mathrm{c}(t)$.

Another method to obtain the forced position operator in Eq. (B1) is to use perturbation theory. The perturbation term $V(t)$ in Eq. (1) for mode m can be expressed as

$$\begin{aligned} V(t) &= -\sum_{m=1}^{2}\boldsymbol{F}(t)\cdot\boldsymbol{b}^m(t)\frac{x_0^m}{Z_m}(e^{i\omega_m t}a_m^\dagger + e^{-i\omega_m t}a_m) \\ &\approx -\sum_{m=1}^{2}\boldsymbol{F}(t)\cdot\boldsymbol{b}_0^m\frac{x_0^m}{Z_m}(e^{i\omega_m t}a_m^\dagger + e^{-i\omega_m t}a_m), \end{aligned} \quad \text{(B4)}$$

where the oscillating term $\boldsymbol{b}_1^m\cos(\omega_\mathrm{rf}t)$ has been neglected because it leads to terms proportional to q^2 in the final expression. Then the Magnus expansion results in the propagator

$$\begin{aligned} U(t) &= \prod_{m=1}^{2}e^{-i\Phi_m(t)}D[\alpha_m^{(1)}(t)], \\ \alpha_m^{(1)}(t) &= \frac{i}{\hbar}x_0^m\int_0^t dt_1 e^{i\omega_m t_1}\boldsymbol{F}(t_1)\cdot\boldsymbol{b}_0^m, \\ \Phi_m(t) &= \frac{1}{\hbar^2}x_0^{m2}\int_0^t dt_1[\boldsymbol{F}(t_1)\cdot\boldsymbol{b}_0^m] \\ &\quad\times\int_0^{t_1}dt_2[\boldsymbol{F}(t_2)\cdot\boldsymbol{b}_0^m]\sin[\omega_m(t_2-t_1)]. \end{aligned} \quad \text{(B5)}$$

Acting $U(t)$ on Eq. (A7), we get the forced position operator in the Heisenberg picture as

$$\begin{aligned} \boldsymbol{x}_\mathrm{q}(t) &= U^\dagger(t)\boldsymbol{x}(t)U(t) \\ &= \sum_{m=1}^{2}\frac{\boldsymbol{b}^m(t)}{Z_m}x_0^m\{e^{i\omega_m t}a_m^\dagger + e^{-i\omega_m t}a_m + 2\,\mathrm{Re}[\tilde{\alpha}_m(t)]\}, \end{aligned} \quad \text{(B6)}$$

where $\tilde{\alpha}_m(t) = e^{-i\omega_m t}\alpha_m^{(1)}(t) = \alpha_m(t) - e^{-i\omega_m t}\alpha_m(0)$, with $\alpha_m(t)$ from Eq. (B3). It can be shown that Eq. (B6) is equivalent to Eq. (B1) by substituting $a_m^\dagger = A_m^\dagger + \alpha_m^*(0)$ and $a_m = A_m + \alpha_m(0)$ into Eq. (B6). Therefore, we can use either a_m or A_m, depending on the context. Note that at instance $t = 0$, the oscillator states $|n_m\rangle_{A_m}$ and $|n_m\rangle_{a_m}$, where the subscripts denote the operators with respect to which the states are defined, are related by $|n_m\rangle_{A_m} = D(\alpha_m)|n_m\rangle_{a_m}$ [26]. In particular, $|0_m\rangle_{A_m} = |\alpha_m\rangle_{a_m}$ since $A_m|0_m\rangle_{A_m} = (a_m - \alpha_m)|\alpha_m\rangle_{a_m} = (\alpha_m - \alpha_m)|\alpha_m\rangle_{a_m} = 0$. The basis set $\{|n_m\rangle_{A_m}\}$ can actually be interpreted as a set of dressed states in the presence of the external force $\boldsymbol{F}(t)$.

APPENDIX C: LIGHT-ATOM INTERACTIONS

Let us consider the commonly used Hamiltonian of a trapped ion, which contains an internal two-level system and motional degree of freedom, coupled by an external radiation field. In the interaction picture of the two-level system, the Hamiltonian can be expressed as [9]

$$H_\mathrm{LA}(t) = H(t) + \frac{\hbar\Omega}{2}(e^{i\boldsymbol{k}\cdot\boldsymbol{x}(t)}e^{-i\phi(t)}\sigma_+ + \mathrm{H.c.}), \quad \text{(C1)}$$

where $H(t)$ is the Hamiltonian of the ion motion in Eq. (1), and the definition of the parameters and operators are given in Sec. II C. If we assume that the radiation field does not drive transitions between the oscillator states, we can go into the interaction picture with respect to the entire Hamiltonian $H(t)$, through which the Hamiltonian is transformed as

$$H'_\mathrm{LA}(t) = \frac{\hbar\Omega}{2}(e^{i\boldsymbol{k}\cdot\boldsymbol{x}_\mathrm{q}(t)}e^{-i\phi(t)}\sigma_+ + \mathrm{H.c.}), \quad \text{(C2)}$$

where $\boldsymbol{x}_\mathrm{q}(t)$ is from either Eq. (B1) or (B6). As in Appendix B, it is possible to use either $|n_m\rangle_{A_m}$ or $|n_m\rangle_{a_m}$, given the right initial conditions. On the other hand, if significant transitions between oscillator states are induced by the external field, i.e., the detuning is close to the resonant frequency of the oscillator modes, then the states $\{|n_m\rangle_{A_m}\}$ do not serve as a good basis because the perturbation due to the radiation field may become comparable to $V(t)$ in Eq. (1). In this case, we must solve the effective Hamiltonian

$$H'_\mathrm{LA}(t) = -\boldsymbol{F}(t)\cdot\boldsymbol{x}(t) + \frac{\hbar\Omega}{2}(e^{i\boldsymbol{k}\cdot\boldsymbol{x}(t)}e^{-i\phi(t)}\sigma_+ + \mathrm{H.c.}), \quad \text{(C3)}$$

where $\boldsymbol{x}(t)$ is the position operator in Eq. (A7), with the unperturbed basis being $\{|n_m\rangle_{a_m}\}$. Since this work is mainly focused on the carrier transition, which does not involve transitions between oscillator states, the effective Hamiltonian (C2) is a good approximation.

APPENDIX D: TWO-DIMENSIONAL DISPLACEMENT SCAN WITH RESPECT TO THE DOPPLER/SPAM BEAM

The experimental results of the two-dimensional displacement scan corresponding to the simulation results in row (4) of Fig. 2 are presented in Fig. 4. Rows (0) and (3) are identical to rows (0) and (4) of Fig. 2, shown for convenience. In row (0), the Doppler/SPAM beam is detuned by −22 MHz, the rf frequency, from the cooling transition during Doppler cooling, while in row (1), it is detuned by −10 MHz, the optimal Doppler cooling condition.

Here we elaborate on the measurement of $P_{\downarrow,\mathrm{SPAM}}$, which can be extracted by conducting state detection immediately after Doppler cooling. Experimentally, it is the probability to correctly detect the fluorescing ion as the state $|\downarrow\rangle$. To comprehend the full picture including photon scattering, consider the schematic energy-level diagram shown in Fig. 5 [31], with the states $|\uparrow\rangle$ and $|\downarrow\rangle$ in the S orbital and $|e\rangle$ in the P orbital. In realistic conditions, various sidebands are present and different states in the S and P orbitals are involved in each step of state preparation and measurement, but the simplistic depiction in Fig. 5 is sufficient for our purposes.

Let us assume a two-level system composed of the states $|\downarrow\rangle$ and $|e\rangle$, where the decay rate of $|e\rangle$ is given as Γ. When

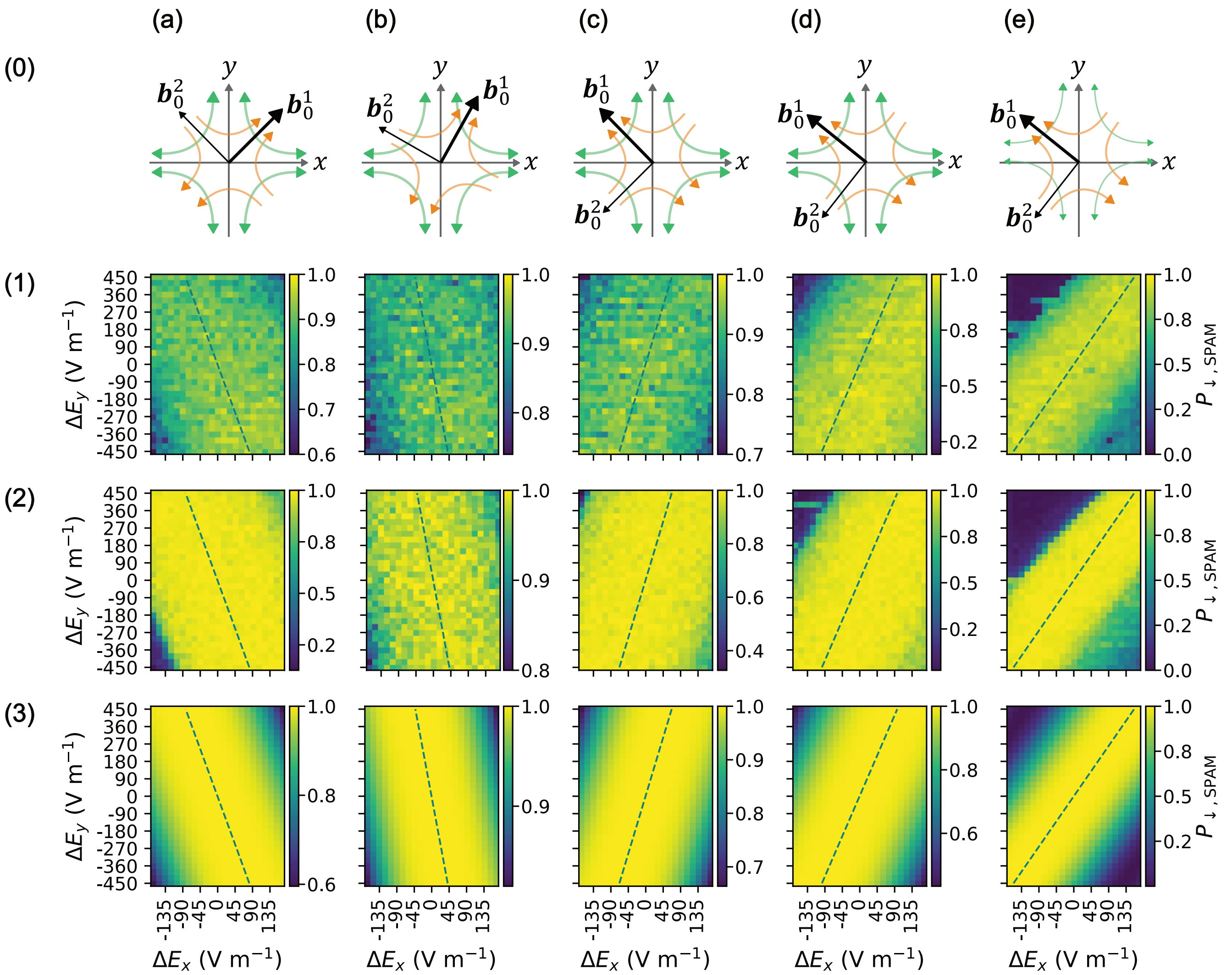

FIG. 4. Results of the two-dimensional displacement scan with the Doppler/SPAM beam. Columns (a)–(e) categorize results based on different potential configurations, while rows (0)–(3) present results obtained under identical conditions, differing only in the potential configuration. For each column, the secular frequencies and potential rotation angles are (a) $\{\omega_1, \omega_2\}/2\pi = \{1.79(0), 2.14(6)\}$ MHz and $\theta \approx \pi/4$, (b) $\{\omega_1, \omega_2\}/2\pi = \{1.87(4), 2.07(3)\}$ MHz and $\theta \approx \pi/3$, (c) $\{\omega_1, \omega_2\}/2\pi = \{1.82(0), 2.12(1)\}$ MHz and $\theta \approx 3\pi/4$, (d) $\{\omega_1, \omega_2\}/2\pi = \{1.75(6), 2.22(6)\}$ MHz and $\theta \approx 7\pi/9$, and (e) $\{\omega_1, \omega_2\}/2\pi = \{1.26(8), 1.88(2)\}$ MHz and $\theta \approx 7\pi/9$. Only the dc voltages have been varied in (a)–(d), while in (e), the rf voltage amplitude has been reduced by a factor of 0.8, keeping the dc voltages identical to those in (d). Row (0) shows the schematic depiction of potential configurations. The data in the subsequent rows are given as follows: experimental data of the scan with the Doppler/SPAM beam detuned by (1) -22 MHz and (2) -10 MHz from the cooling transition during Doppler cooling and (3) simulation data of the scan conducted with the Doppler/SPAM beam, $P_{\downarrow,\mathrm{SPAM}}$. The theoretical rf pseudonull lines induced by the Doppler/SPAM beam are represented by teal dashed lines.

light drives transitions between the two states at a rate given by Ω, the steady-state population of the state $|e\rangle$ is derived as [38]

$$P_e(t \to \infty) = \frac{1}{2}\frac{s}{1+s}, \quad s \approx \frac{2(\tilde{\Omega}/\Gamma)^2}{1+(2\Delta/\Gamma)^2}, \tag{D1}$$

where $\tilde{\Omega} = J_0(\beta)\Omega$ denotes the modified Rabi frequency, parametrized by the Bessel function of type zero and the modulation depth β, in the presence of micromotion at a given displacement. Additionally, we assume $\Delta = 0$ and limit the discussion to carrier transitions. In the typical regime of operation where $\beta = 0$ and $\Omega \gg \Gamma$, we have $P_e(t \to \infty) \approx 1/2$ in the steady state. On the other hand, when the net phase modulation from micromotion is significant, $\beta \gg 1$ and $\tilde{\Omega} \ll \Gamma$, we get $P_e(t \to \infty) \propto |\tilde{\Omega}|^2$, varying with the value of β. This is graphically visualized in the plot of $P_e(t)$ at the center of Fig. 5. The transient response of $P_e(t)$, represented as the shaded area in light purple, is generally inaccessible during experiments due to the large decay rate $\Gamma/2\pi \approx 20$ MHz. During detection, the ion's fluorescence is collected for a fixed exposure time, indicated as T_{exp} in Fig. 5, and the resulting Poisson distribution of photon counts is used for state discrimination between $|\uparrow\rangle$ and $|\downarrow\rangle$ [31]. Recall that $\epsilon = 1 - P_{\downarrow,\mathrm{SPAM}}$ is not equivalent to the probability of detecting $|\uparrow\rangle$, as the ion is always fluorescing by

TABLE I. Numerical values of the parameters used for the potential configurations in the simulation of the two-dimensional displacement scan.

Parameter	(a)	(b)	(c)	(d)	(e)
α (cm^{-2})	-980	-550	-850	-1370	-1370
β, γ (cm^{-2})	134, 2200				
V_{dc} (V)	5				
V_{rf} (V)	200				160
θ (rad)	$\pi/4$	$\pi/3$	$3\pi/4$	$7\pi/9$	$7\pi/9$
$\omega_1/2\pi$ (MHz)	1.79(0)	1.87(4)	1.82(0)	1.75(6)	1.26(8)
$\boldsymbol{b}_0^1$	(0.707, 0.707)	(0.497, 0.868)	$(-0.707, 0.707)$	$(-0.767, 0.642)$	$(-0.767, 0.642)$
$\boldsymbol{b}_1^1$	$(0.045, -0.045)$	$(0.0316, -0.0551)$	$(-0.045, -0.045)$	$(-0.0496, -0.0416)$	$(-0.0397, -0.0333)$
$\omega_2/2\pi$ (MHz)	2.14(6)	2.07(3)	2.12(1)	2.22(6)	1.88(2)
$\boldsymbol{b}_0^2$	$(0.707, -0.707)$	$(0.868, -0.497)$	$(-0.707, -0.707)$	(0.642, 0.767)	(0.642, 0.767)
$\boldsymbol{b}_1^2$	(0.045, 0.045)	(0.0551, 0.0316)	$(-0.045, 0.045)$	$(0.0416, -0.0496)$	$(0.0333, -0.0397)$
$x_{\max}$ (μm)	± 307	± 279	± 304	± 315	± 556
$y_{\max}$ (μm)	± 838	± 898	± 830	± 798	± 1336

transitioning between $|{\downarrow}\rangle$ and $|e\rangle$ in the steady state. However, since the two cases are experimentally indistinguishable, the standard state detection scheme can measure $P_{\downarrow,\mathrm{SPAM}}$ from the observed intensity variations of fluorescence.

Clearly, the patterns of $P_{\downarrow,\mathrm{SPAM}}$, obtained from both the system Hamiltonian simulation and the more realistic model incorporating scattering, are predominantly governed by the same displacement-dependent variation in Rabi frequencies. In the latter, which relates more directly to the observed quantity, $P_{\downarrow,\mathrm{SPAM}}$ may be seen as a map from the domain (0,0.5) of P_e to the codomain (0,1.0), scaled by the micromotion-modified Rabi frequency, as shown in Fig. 5. Our claim is supported by the excellent agreement of the experimental data of $P_{\downarrow,\mathrm{SPAM}}$ in rows (1) and (2) of Fig. 4 with the simulation results in row (3). When the ion is located along the rf pseudonull line induced by the Doppler/SPAM beam, the fluorescence is largest, i.e., $P_{\downarrow,\mathrm{SPAM}} = 1$, leading to efficient Doppler cooling and higher detection fidelity. However, when it is displaced from the pseudonull and $\phi_{\mathrm{ex}}(t) \neq 0$, the value of $P_{\downarrow,\mathrm{SPAM}}$ decreases, preventing the ion from reaching the Doppler limit [10] and resulting in larger measurement errors.

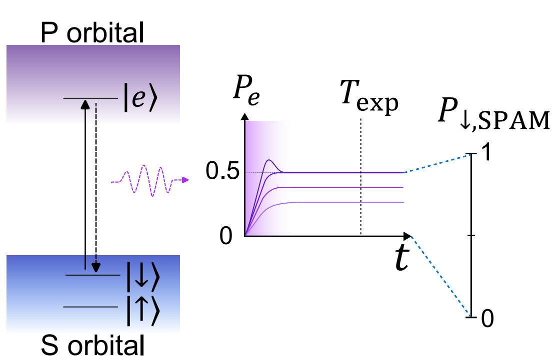

FIG. 5. Schematic depiction of the derivation of $P_{\downarrow,\mathrm{SPAM}}$. On the left, the internal states $|{\uparrow}\rangle$ and $|{\downarrow}\rangle$ and the state $|e\rangle$, used for the dissipative scattering processes, are visualized in the S and P orbitals, respectively. The Doppler/SPAM beam drives transitions between $|{\downarrow}\rangle$ and $|e\rangle$. The population of $|e\rangle$, $P_e(t)$, saturates at a level set by the Rabi frequency modified by micromotion, $\tilde{\Omega}$, and the decay rate of $|e\rangle$, given by Γ. Its maximum value is 1/2 and decreases as $\tilde{\Omega}$ is reduced, as shown at the center of the figure. The steady-state value $P_e(t \to \infty)$ is translated into the probability used for state detection, $P_{\downarrow,\mathrm{SPAM}}$, with the scaling factor directly determined by the Rabi frequency modified by micromotion.

The rf pseudonull induced by the Doppler/SPAM beam can clearly be seen throughout Figs. 4(a)–4(e), with the relative strengths between different displacement values in good agreement with simulation results. There are however regions where $P_{\downarrow,\mathrm{SPAM}}$ drops dramatically to near zero in all cases. We observe a significant increase in the overall ion motion in these regions, detectable via the electron-multiplying charge-coupled device used for ion imaging. Our conjecture is that, due to inefficient Doppler cooling in these areas, the ion image becomes blurred, resulting in a significant loss in fluorescence. These effects are noticeably reduced when the Doppler/SPAM beam is tuned to the rf frequency, as shown in row (1), rather than under optimal Doppler cooling conditions in row (2), consistently explaining the results in Fig. 2. Note that the detection fidelity is slightly lower in row (1) compared to row (2) due to constraints in the optical devices, but this does not compromise the validity of the experimental data.

APPENDIX E: SIMULATION PARAMETERS

Numerical values of the parameters used for the simulations in Figs. 2 and 4 are listed in Table I. Columns (a)–(e) label different potential configurations. The secular-micromotion modes $\{\omega_m, \boldsymbol{b}_0^m, \boldsymbol{b}_1^m\}$ are obtained from the parameters listed in the top five rows. The maximum displacements of the ion $x_{\max}$ and $y_{\max}$, induced by the control electric fields ΔE_x and ΔE_y, are given in the last row in terms of spatial units. They are well within the spatial extent of the beam width and Rayleigh range of the lasers used for experimentation. Note that calculations have been conducted in cgs units. The potential rotation θ and magnitude of the control electric fields ΔE_x and ΔE_y have been extracted from COMSOL, whereas the secular frequencies ω_1 and ω_2 have been measured through sideband scans via the Raman transition [9].

[1] S. A. Moses, C. H. Baldwin, M. S. Allman, R. Ancona, L. Ascarrunz, C. Barnes, J. Bartolotta, B. Bjork, P. Blanchard, M. Bohn *et al.*, A race-track trapped-ion quantum processor, Phys. Rev. X **13**, 041052 (2023).

[2] J.-S. Chen, E. Nielsen, M. Ebert, V. Inlek, K. Wright, V. Chaplin, A. Maksymov, E. Páez, A. Poudel, P. Maunz, and J. Gamble, Benchmarking a trapped-ion quantum computer with 30 qubits, Quantum **8**, 1516 (2024).

[3] K. Mayer, C. Ryan-Anderson, N. Brown, E. Durso-Sabina, C. H. Baldwin, D. Hayes, J. M. Dreiling, C. Foltz, J. P. Gaebler, T. M. Gatterman *et al.*, Benchmarking logical three-qubit quantum Fourier transform encoded in the Steane code on a trapped-ion quantum computer, arXiv:2404.08616v1.

[4] C. Monroe, W. C. Campbell, L.-M. Duan, Z.-X. Gong, A. V. Gorshkov, P. W. Hess, R. Islam, K. Kim, N. M. Linke, G. Pagano *et al.*, Programmable quantum simulations of spin systems with trapped ions, Rev. Mod. Phys. **93**, 025001 (2021).

[5] S.-A. Guo, Y.-K. Wu, J. Ye, L. Zhang, W.-Q. Lian, R. Yao, Y. Wang, R.-Y. Yan, Y.-J. Yi, Y.-L. Xu *et al.*, A site-resolved two-dimensional quantum simulator with hundreds of trapped ions, Nature (London) **630**, 613 (2024).

[6] Y. Lu, W. Chen, S. Zhang, K. Zhang, J. Zhang, J.-N. Zhang, and K. Kim, Implementing arbitrary Ising models with a trapped-ion quantum processor, Phys. Rev. Lett. **134**, 050602 (2025).

[7] S. Auchter, C. Axline, C. Decaroli, M. Valentini, L. Purwin, R. Oswald, R. Matt, E. Aschauer, Y. Colombe, P. Holz *et al.*, Industrially microfabricated ion trap with 1 eV trap depth, Quantum Sci. Technol. **7**, 035015 (2022).

[8] R. F. Spivey, I. V. Inlek, Z. Jia, S. Crain, K. Sun, J. Kim, G. Vrijsen, C. Fang, C. Fitzgerald, S. Kross *et al.*, High-stability cryogenic system for quantum computing with compact packaged ion traps, IEEE Trans. Quantum Eng. **3**, 1 (2022).

[9] D. Leibfried, R. Blatt, C. Monroe, and D. Wineland, Quantum dynamics of single trapped ions, Rev. Mod. Phys. **75**, 281 (2003).

[10] D. J. Berkeland, J. D. Miller, J. C. Bergquist, W. M. Itano, and D. J. Wineland, Minimization of ion micromotion in a Paul trap, J. Appl. Phys. **83**, 5025 (1998).

[11] S.-L. Zhu, C. Monroe, and L.-M. Duan, Trapped ion quantum computation with transverse phonon modes, Phys. Rev. Lett. **97**, 050505 (2006).

[12] Y.-H. Hou, Y.-J. Yi, Y.-K. Wu, Y.-Y. Chen, L. Zhang, Y. Wang, Y.-L. Xu, C. Zhang, Q.-X. Mei, H.-X. Yang *et al.*, Individually addressed entangling gates in a two-dimensional ion crystal, Nat. Commun. **15**, 9710 (2024).

[13] F. Diedrich and H. Walther, Nonclassical radiation of a single stored ion, Phys. Rev. Lett. **58**, 203 (1987).

[14] Y. Ibaraki, U. Tanaka, and S. Urabe, Detection of parametric resonance of trapped ions for micromotion compensation, Appl. Phys. B **105**, 219 (2011).

[15] B. L. Chuah, N. C. Lewty, R. Cazan, and M. D. Barrett, Detection of ion micromotion in a linear Paul trap with a high finesse cavity, Opt. Express **21**, 10632 (2013).

[16] J. Keller, H. L. Partner, T. Burgermeister, and T. E. Mehlstäubler, Precise determination of micromotion for trapped-ion optical clocks, J. Appl. Phys. **118**, 104501 (2015).

[17] L. A. Zhukas, M. J. Millican, P. Svihra, A. Nomerotski, and B. B. Blinov, Direct observation of ion micromotion in a linear Paul trap, Phys. Rev. A **103**, 023105 (2021).

[18] C. J. B. Goham and J. W. Britton, Resolved-sideband micromotion sensing in Yb^+ on the 935 nm repump transition, AIP Adv. **12**, 115315 (2022).

[19] W. Lee, D. Chung, J. Kang, H. Jeon, C. Jung, D.-I. D. Cho, and T. Kim, Micromotion compensation of trapped ions by qubit transition and direct scanning of dc voltages, Opt. Express **31**, 33787 (2023).

[20] C. W. Hogle, A. D. Burch, J. D. Sterk, M. N. H. Chow, M. Ivory, D. S. Lobser, P. Maunz, J. Van Der Wall, C. G. Yale, S. M. Clark *et al.*, Precise micromotion compensation of a tilted ion chain, Front. Quantum Sci. Technol. **3**, 1352800 (2024).

[21] K. J. Arnold, N. Jayjong, M. L. D. Kang, Q. Qichen, Z. Zhang, Q. Zhao, and M. D. Barrett, Enhanced micromotion compensation using a phase-modulated light field, Phys. Rev. A **110**, 033115 (2024).

[22] L. H. Nguyên, A. Kalev, M. D. Barrett, and B.-G. Englert, Micromotion in trapped atom-ion systems, Phys. Rev. A **85**, 052718 (2012).

[23] H. R. Lewis, Jr. and W. B. Riesenfeld, An exact quantum theory of the time-dependent harmonic oscillator and of a charged particle in a time-dependent electromagnetic field, J. Math. Phys. **10**, 1458 (1969).

[24] R. J. Glauber, in *Foundations of Quantum Mechanics*, edited by T. D. Black, M. M. Nieto, M. O. Scully, R. M. Sinclair, and H. S. Pilloff (World Scientific, Singapore, 1992), pp. 23–39.

[25] J.-Y. Ji, J. K. Kim, and S. P. Kim, Heisenberg-picture approach to the exact quantum motion of a time-dependent harmonic oscillator, Phys. Rev. A **51**, 4268 (1995).

[26] H.-C. Kim, M.-H. Lee, J.-Y. Ji, and J. K. Kim, Heisenberg-picture approach to the exact quantum motion of a time-dependent forced harmonic oscillator, Phys. Rev. A **53**, 3767 (1996).

[27] M. G. House, Analytic model for electrostatic fields in surface-electrode ion traps, Phys. Rev. A **78**, 033402 (2008).

[28] D. T. C. Allcock, J. A. Sherman, D. N. Stacey, A. H. Burrell, M. J. Curtis, G. Imreh, N. M. Linke, D. J. Szwer, S. C. Webster, A. M. Steane, and D. M. Lucas, Implementation of a symmetric surface-electrode ion trap with field compensation using a modulated Raman effect, New J. Phys. **12**, 053026 (2010).

[29] S. Hong, M. Lee, H. Cheon, T. Kim, and D.-I. D. Cho, Guidelines for designing surface ion traps using the boundary element method, Sensors **16**, 616 (2016).

[30] D. Chung, K. Choi, W. Lee, C. Kim, H. Shon, J. Park, B. Cho, K. Lee, S. Kim, S. Yoo, U. Jung, C. Jung, J. Kang, K. Kim, R. Berkis, T. Northup, D.-I. D. Cho, and T. Kim, A silicon-based ion trap chip protected from semiconductor charging, Quantum Sci. Technol. **10**, 035014 (2025).

[31] S. Olmschenk, K. C. Younge, D. L. Moehring, D. N. Matsukevich, P. Maunz, and C. Monroe, Manipulation and detection of a trapped Yb^+ hyperfine qubit, Phys. Rev. A **76**, 052314 (2007).

[32] J. Mizrahi, B. Neyenhuis, K. G. Johnson, W. C. Campbell, C. Senko, D. Hayes, and C. Monroe, Quantum control of qubits and atomic motion using ultrafast laser pulses, Appl. Phys. B **114**, 45 (2014).

[33] J. P. Gaebler, C. H. Baldwin, S. A. Moses, J. M. Dreiling, C. Figgatt, M. Foss-Feig, D. Hayes, and J. M. Pino, Suppression of midcircuit measurement crosstalk errors with micromotion, Phys. Rev. A **104**, 062440 (2021).

[34] N. K. Lysne, J. F. Niedermeyer, A. C. Wilson, D. H. Slichter, and D. Leibfried, Individual addressing and state readout of trapped ions utilizing radio-frequency micromotion, Phys. Rev. Lett. **133**, 033201 (2024).

[35] J. I. Cirac, L. J. Garay, R. Blatt, A. S. Parkins, and P. Zoller, Laser cooling of trapped ions: The influence of micromotion, Phys. Rev. A **49**, 421 (1994).

[36] J. Eschner, G. Morigi, F. Schmidt-Kaler, and R. Blatt, Laser cooling of trapped ions, J. Opt. Soc. Am. B **20**, 1003 (2003).

[37] S. A. Schulz, U. Poschinger, F. Ziesel, and F. Schmidt-Kaler, Sideband cooling and coherent dynamics in a microchip multi-segmented ion trap, New J. Phys. **10**, 045007 (2008).

[38] R. G. DeVoe, J. Hoffnagle, and R. G. Brewer, Role of laser damping in trapped ion crystals, Phys. Rev. A **39**, 4362 (1989).

[39] R. Dum, P. Zoller, and H. Ritsch, Monte Carlo simulation of the atomic master equation for spontaneous emission, Phys. Rev. A **45**, 4879 (1992).

[40] C. Gardiner and P. Zoller, *The Quantum World of Ultra-Cold Atoms and Light. Book II: The Physics of Quantum-Optical Devices*, 1st ed., Cold Atoms Vol. 4 (Imperial College Press, London, 2015), Chap. 10.

[41] J. Javanainen and S. Stenholm, Laser cooling of trapped particles I: The heavy particle limit, Appl. Phys. **21**, 283 (1980).

[42] A. Bermudez, P. Schindler, T. Monz, R. Blatt, and M. Müller, Micromotion-enabled improvement of quantum logic gates with trapped ions, New J. Phys. **19**, 113038 (2017).

[43] G. Higgins, S. Salim, C. Zhang, H. Parke, F. Pokorny, and M. Hennrich, Micromotion minimization using Ramsey interferometry, New J. Phys. **23**, 123028 (2021).

[44] J. Keller, D. Kalincev, T. Burgermeister, A. P. Kulosa, A. Didier, T. Nordmann, J. Kiethe, and T. E. Mehlstäubler, Probing time dilation in Coulomb crystals in a high-precision ion trap, Phys. Rev. Appl. **11**, 011002(R) (2019).

[45] Y. Huang, H. Guan, M. Zeng, L. Tang, and K. Gao, $^{40}Ca^{+}$ ion optical clock with micromotion-induced shifts below 1×10^{-18}, Phys. Rev. A **99**, 011401(R) (2019).

[46] W. Lee, D. Chung, H. Jeon, B. Cho, K. Choi, S. Yoo, C. Jung, J. Jeong, C. Kim, D.-I. D. Cho, and T. Kim, Photoinduced charge-carrier dynamics in a semiconductor-based ion trap investigated via motion-sensitive qubit transitions, Phys. Rev. A **109**, 043106 (2024).